Pattern selection of directionally oriented chitosan tubes

Cintia Hajdu,[1, a)] Pawan Kumar,[1, a)] Dezső Horváth,[2] and Ágota Tóth[1]
[1)]*Department of Physical Chemistry and Materials Science, University of Szeged, Rerrich Béla tér 1., Szeged, H-6720, Hungary.*
[2)]*Department of Applied and Environmental Chemistry, University of Szeged, Rerrich Béla tér 1., Szeged, H-6720, Hungary.*

(*Electronic mail: atoth@chem.u-szeged.hu)

(Dated: 17 March 2022)

The growth of viscoelastic curved materials, inspired by biological systems, may give rise to various complex structures. One of the simplest ways to control the pattern formation is to vary the orientation of the reaction vessel, while keeping all other experimental conditions constant. Here we report the self-organization of soft chitosan tubes by injecting acidic chitosan sol into a pool of sodium hydroxide solution, where the adhesive force between the gel and container keeps the tubules on the bottom of the reactor. The horizontal growth of the tubular structure undergoes spontaneous symmetry breaking, where instabilities develop on the surface of the chitosan tubules. Transformation of folds into wrinkles and finally to a smooth tube takes place by varying the orientation of the container. Besides characterizing the evolving structures, we have also shown that the linear growth rate of the tube scales with the tilt angle of the container from the horizontal.

I. INTRODUCTION

Systems far from equilibrium may give rise to self-assembly of spatiotemporal complex structures.[1–4] The chemo-mechanical forces like buoyancy, osmosis, chemical potential gradient, and the driving force arising from injection or from the presence of external electric[2] and/or magnetic fields[2,5] control the structural formations besides chemical interactions. Tubular morphologies can be developed in three-dimensional space,[6–9] while in quasi-two-dimensional reaction vessels filamental shapes can grow.[10,11] These formations are not limited to inorganic materials. Metal-ion organic gardens, for example iron(III) oleate, have been produced in polar organic solvent such as isopropanol.[12] Hydrogel tubes[13] along with inorganic composites[14–16] are also explored via flow-injection techniques, where the adhesive nature of the gel aids in guiding the soft tubules.

Interestingly, the flexible nature of soft materials allows the deformation of various structural shapes and patterns under mechanical forces. Due to the gradients[17] and compressive stress in the presence of solvents[18] and external stimuli like temperature[19,20] or photo illumination[21,22], symmetry breaking occurs on smooth surfaces, resulting in buckling instabilities. From the past few decades, in laboratory systems, buckling has been observed in a wide range of length scales[23,24] supporting fabrications of nano- and microscale devices. In particular, wrinkle patterns appear at small compression, which is largely explored in case of planar membranes due to the ease of the membrane creation.[25,26] However, larger strain induces nonlinearity in the membrane, under which localization of wrinkles into folds takes place.[27–31] Physical systems are rich in complex patterns like wrinkles of human skin and folding in plants[32,33]. The creation and the transformation of patterns are also helpful for functioning biological systems: the folding of the brain's cerebral cortex improves its efficiency[34], and the wrinkles in the intestine enhance digestion,[35] just to name a few.

In the real world, from natural to biological systems, structures determine the three-dimensional curvature, and the geometric constraints of curved materials facilitate the formation of complex patterns.[36] Therefore it is fundamental to study the surface instabilities on artificial curved surfaces for understanding the mechanism of deformations. Most of these formations are explored experimentally on prefabricated elastic materials and much less is known when buckling instabilities develop via self-organization. A typical way to control pattern formation is to tune material compositions and/or mechanical forces. For example it has been found that the growth of biological tubular membranes enhances the strain under which a wide variety of surface patterns appears: thin-walled hollow materials can develop longitudinal or circumferential patterns like folding in eosinophilic esophagitis.[37]

We have introduced a flow-injection technique to design self-assembled chitosan (CS) tubules which grow vertically.[13] The hydrogel forms via sol-gel transition based upon the pH of the reaction matrix. Various periodic and aperiodic deformations in the form of folding and wrinkling can occur on the surface when the growth is along a glass vessel depending on the chemical composition and the flow rate.[38] In the current work, we show that we can control the pattern selection by only varying the container orientation and keeping all other experimental conditions constant. Furthermore, a scaling law, describing the dependence of growth rate with respect to the orientation, is derived besides the detailed characterization of the evolving patterns.

II. EXPERIMENTAL

Analytical grade reagents, low (LMW) and medium (MMW) molecular weight of chitosan (Sigma-Aldrich 448869 and 448877, respectively), CH_3COOH (VWR, 99-100 %), and NaOH (Sigma-Aldrich, pellets), were used for

[a)]These two authors contributed equally

all experiments. CS (LMW or MMW) sol with concentration of 0.75 w/V % in 0.2 M acetic acid solution was prepared by stirring overnight. A flow-driven system was implemented to observe the surface instabilities of the CS hydrogel. Figure 1 shows the schematic diagram, where CS solution was injected from below with a syringe pump through a plastic tube and inlet needle (i.d. 0.4 mm) into the alkaline solutions with concentrations of 0.75 M or 1.5 M. With these concentrations the density decrease due to the heat of neutralization, estimated from the adiabatic temperature rise, is significantly smaller ($< 5\%$) than the existing difference between the two liquids.

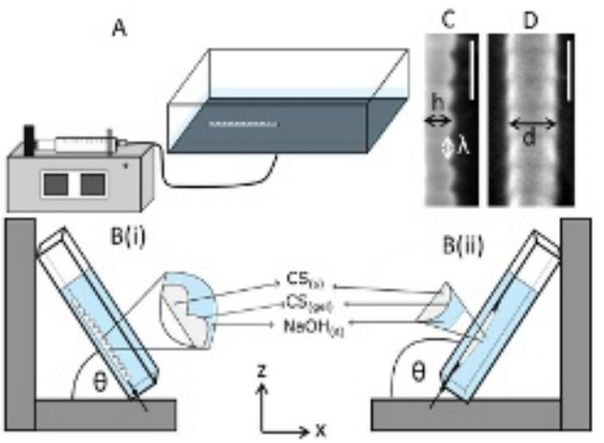

FIG. 1. Schematic diagram of the flow-driven system: (A) represents the horizontal configuration and (B) the inclined scheme with (i) $\theta < 90^\circ$ and (ii) $\theta > 90^\circ$. Images C and D depict the side (C) and front (D) view of the patterns to indicate tube depth (h), diameter (d) and wavelength (λ) with the scale bars representing 0.5 cm.

In the present study, we grow chitosan tubes on horizontal and inclined surfaces. Figure 1A displays the experimental setup for the horizontal configuration, where a glass container of dimensions $15 \times 15 \times 5$ cm^3 was filled with 150 mL alkaline solution. The injected flow rate, Q, of the CS solutions was varied between 0.1 – 0.8 mL min^{-1}. For the inclined orientations (see Fig. 1B), we used a plexiglass cuvette of inner dimensions $2 \times 1 \times 10$ cm, and the flow rate from the syringe pump was maintained at 0.6 mL min^{-1}. The tilt angle of the container, θ, with respect to the horizontal (see Fig. 1B) was varied by changing the horizontal and vertical distances from the wall. Experiments were performed at room temperature 24 $\pm$ 1 °C. A Vivitar CCD camera was vertically mounted sufficiently far from the setup, allowing the reconstruction of images at various tilt angles because surface deformations were small. The camera was connected to a computer to record images of the pattern formation. The characteristic properties of the tubes were calculated by the ImageJ software, similar to our previous work.[13,38]

III. RESULTS AND DISCUSSION

A. Growth on horizontal surface

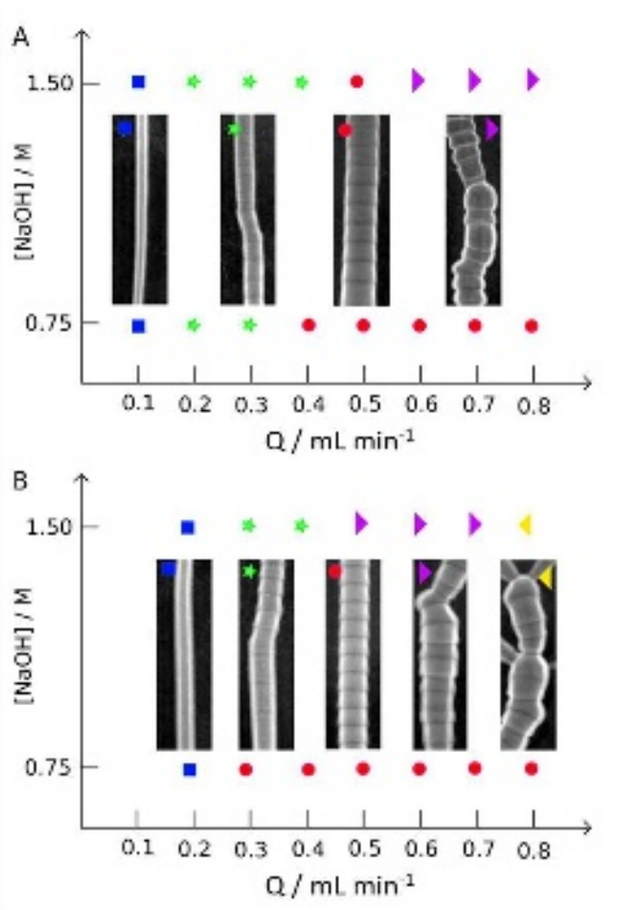

FIG. 2. Dynamical phase diagram of the surface patterning on chitosan tubules for (A) LMW and (B) MMW. The field view of all images is 0.75×2.59 cm^2.

When the acidic CS solution is injected into the alkaline, sol-gel transition immediately occurs at their interface forming a hydrogel membrane and hence separating the acidic and the basic environments into different compartments. The CS solution has lower density than that in the reservoir[38] resulting in an upward growing structure, but the adhesive force between the gel and container keeps the tubules on the bottom of the reactor leading to horizontal growth. Figure 2 summarizes the evolving patterns as a function of the injection rate for both type of hydrogels. The simplest tube structure with smooth outer surface (square markers in Fig. 2) appears at low flow rate. Upon increasing Q, we see that regular folding pattern (circular markers) transverse to tube growth evolves. During the transition of the two structures (star markers), folds deform intermittently on the surface. The greater flow rate carries larger amount of chitosan near the tube head, which increases the inner pressure and causes deviation in the tube

evolution. This process creates irregular folds, and even fractures can occur at the weaker spots (triangular markers). The leakage from the fracture originates a new tubule, which can maintain smooth outer surface or develop folding patterns. The qualitative picture is the same for both types of hydrogels with more branching observed for the MMW gels. (The branching would dominate for high molecular weight gels because of their higher viscosity, which case is not included in this study.) The patterns form right behind the growing head with their wavelength remaining constant on the longer time scale. The gel thickness (30–40 μm) is independent of injection rate; diffusional thickening that smoothens the cusps in the fold structures only takes place on the longer time scale when injection is stopped after the experiments. Then, due to the ultimate thickening of the gel wall, the structure appear brighter.

Image processing aids the characterization of the physical properties of the resultant structures (see definitions in Fig. 1C-D). Figure 3A represents that the linear growth rate (v_ℓ) remains approximately constant, while the tube diameter (d), shown in Fig. 3B, increases as a function of flow rate, independently of the alkaline concentration used. The rise in the

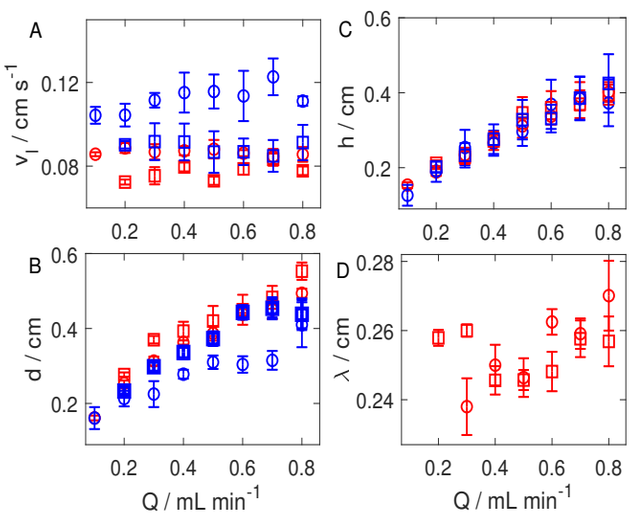

FIG. 3. (A) Velocity v_ℓ, (B) diameter d, (C) depth h of the tube and (D) wavelength λ of the folding patterns as a function of flow rate of LMW (circular markers) and MMW (square markers) hydrogels with $[NaOH]_0$ = 0.75 M (red symbols) and 1.5 M (blue symbols).

NaOH concentration increases the density gradients between the two solution; due to that, at any Q the growth rate increases and the diameter decreases. The volume growth rate, determined as

$$v_V = \frac{\pi d v_\ell h}{4}, \tag{1}$$

is equal to the flow rate Q in the time scale of our experiments.[13,38] The tube depth (h), calculated from this equality, increases monotonically with the flow rates (Fig. 3C). The ratio of tube depth and diameter defined as $R = h/d$ helps in determining the distortion of tubes. For a regular half circle (half tube) $h = d/2$ which yields $R = 0.5$. At greater density gradients, larger elongation takes place in the tube depth resulting in R = 1.00 $\pm$ 0.15 for the LMW and R = 0.85 $\pm$ 0.05 for the MMW polymers. Higher viscosity of the MMW sol increases the cohesive force between the polymer chains, and hence, provides a larger R value for the tubes developed from LMW chitosan than from MMW (see Figure S1 in the SI). The characteristic wavelength (λ) associated with the fold deformation depends on the physical properties of the tubes. We have shown previously[13,38] that for vertically growing tubes the linear growth rate and the wavelength of the patterns increase monotonically with flow rates. However, for a horizontally growing tubule, the increase in d and h maintains a constant v_ℓ resulting in no significant change to the wavelength, as shown in Fig. 3D.

The mechanical stress on the viscoelastic membrane plays a crucial role in the pattern selection. In thin cylinders, where $d/w \gg 1$ with wall thickness w, the internal pressure of fluid p_i exerts the circumferential ($\sigma_\theta = p_i w/2d$) and axial ($\sigma_z = p_i w/4d$) stress. The geometry of the CS tube is comparable with that of the thin cylinder and the propagation of the tube tip also generates axial stress. Nevertheless, the constant tube velocity induces no discernible gain in axial stress, and due to buoyancy, stronger circumference stress acts on the tube resulting in only folding patterns on the curved surface.

B. Growth on inclined surface

We have looked at the effect of orientation for constant experimental conditions. For simplicity we have chosen the LMW chitosan with folding patterns, therefore we have selected injection rate of Q = 0.6 mL min^{-1} with [NaOH] = 0.75 M and varied the tilt angle of the container from the horizontal between 0° and 180°. When the tilt angle lies below 90°, gel layer forms above the lighter acidic solution because the latter advances along the bottom. Figure 4A shows that the CS solution exerts the buoyant force F_b axially as

$$F_\parallel = F_b \sin(\theta) \tag{2}$$

and normally

$$F_\perp = F_b \cos(\theta) \tag{3}$$

to the layer. The former $F_\parallel$ and the latter $F_\perp$ forces support the axial and circumferential stress, respectively. In region (I) of Fig. 4B, $F_\perp$ dominates and creates folding patterns on the surface. Further increasing θ, (region (II) in Fig. 4B), increases $F_\parallel$ resulting in the coexistence of wrinkle and fold modes. Close to 90°, region (III), wrinkling pattern appears with π phase shifts along the boundaries. Above 90° the situation is reversed, i.e., the organized gel layer underlies the CS solution. Force $F_\perp$ acts opposite to the gel, but $F_\parallel$ acts in the same direction. When θ becomes greater than 115°, the decrease in $F_\parallel$ produces thicker tubes, and the wrinkles disappear giving rise to tubes with smooth outer surface (region

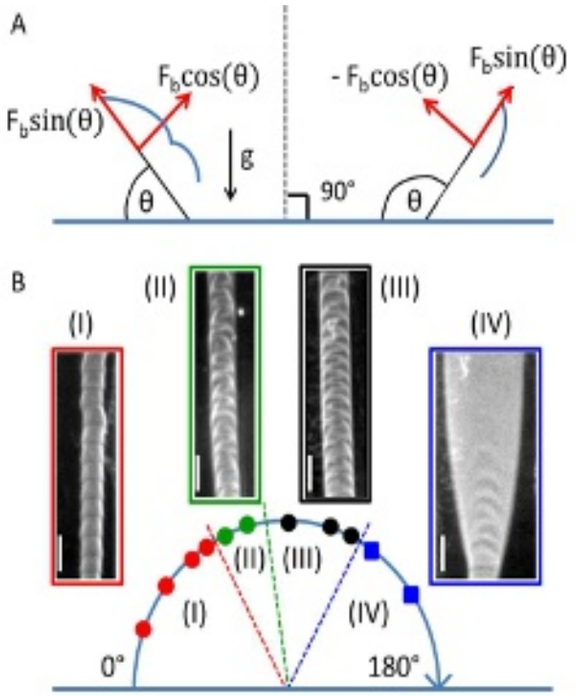

FIG. 4. (A) A schematic to illustrate the buoyant force along the axial ($F_\parallel$) and normal ($F_\perp$) to the tube growth and an arrow indicating the direction of gravity. (B) Surface patterning on the CS tubule (I-IV) as a function of the container orientation for LMW gel with [NaOH] = 0.75 M and Q = 0.6 mL min^{-1} with the scale bars representing 0.5 cm.

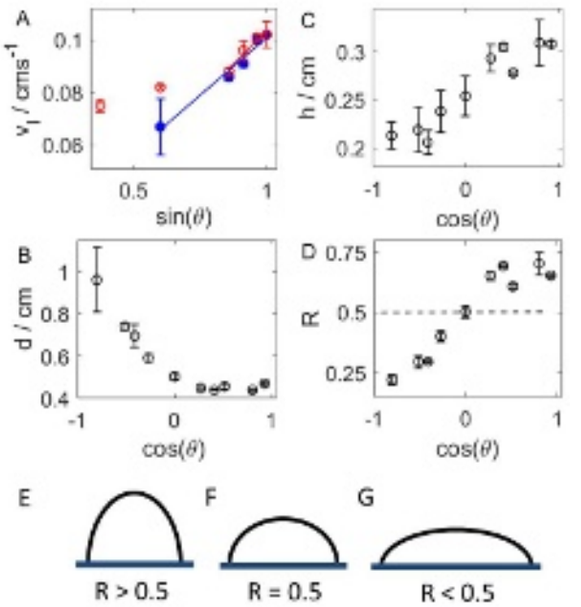

FIG. 5. Characteristic properties of tubes as a function of the orientation: (A) growth velocity v_ℓ vs. $\sin(\theta)$ and (B) depth h, (C) diameter d, and (D) distortion R of the tube vs. $\cos(\theta)$ for LMW gel with Q= 0.6 mL min^{-1}. Schematic (E-F) represent the top view of the tube with (E) $\theta < 90$ °, $\cos\theta > 0$, (F) $\theta = 90$ °, $\cos\theta = 0$, and (G) $\theta > 90°$, $\cos\theta < 0$.

(IV)). The thickness of the membrane does not change significantly by varying the tilt angle.

The characterization of the linear growth velocity, depicted by blue and red colors in Fig. 5A, for angles with $\sin(\theta) > 0.85$ follows a linear scaling as a function of $\sin(\theta)$. The visual inspection of the tube head reveals that simple and/or wrinkling patterned tube propagates with constant curvature. For $\sin(\theta) > 0.85$, $F_\parallel$ dominates, causing a linear dependence of v_ℓ with respect to $\sin(\theta)$ (cf. Eqn. (2)). The buoyant force normal to the tube increases when $\sin(\theta)$ decreases, and, as shown in Fig. 5A with red markers for $\sin(\theta) < 0.85$, divergence occurs from the linear scaling for v_ℓ. Swelling does not play a significant role here either. In our flow-driven system, the fluid flow and the surrounding environment has a vital role in controlling the physical characteristics of the tube. Therefore by considering linear injection rate ($v = Q/A$ where A is the area of the inlet orifice), dynamic viscosity (η) of the injected CS sol, and density gradient $\Delta\rho/\rho_0$ with ρ_0 being the density of the injected CS sol, regardless of the bulk modulus of the membrane, a simplistic dimensional analysis of the tube growth produces the following scaling law

$$v_\ell \propto \frac{g\sin(\theta)\Delta\rho L^2}{\eta}\left(\frac{\eta}{\rho_0 L v}\right)^{(1+\beta)} \tag{4}$$

where L is the characteristic length scale (for example the width of the reaction vessel) and β is an unknown number. By taking advantage of the Reynolds number defined as $\mathrm{Re}=\rho_0 vL/\eta$, and the Archimedes number ($\mathrm{Ar}=g\rho_0\Delta\rho L^3/\eta^2$), equation (4) can be rearranged to the following dimensionless form

$$\frac{v_\ell}{v} \propto \frac{\mathrm{Ar}}{\mathrm{Re}^{(2+\beta)}}\sin(\theta). \tag{5}$$

This scaling law confirms that the linear growth rate of the tubes scales linearly with $\sin(\theta)$ for a given injection rate. We can also suggest values for β as we have observed that the rise in viscosity of the CS solution decreases the growth velocity ($\beta < 0$, Eqn. 4), and increase in the density gradients between the two solutions and the pumping speed increase v_ℓ. Thus, our experimental conditions agree with equations (4) and (5) when β lies in the range of (-2,-1).

We have also determined other tube characteristics: the diameter decreases sharply in the region of $\cos(\theta) \leq 0$ (see Fig. 5B), but no significant change occurs above 0. The depth (Fig. 5C) of the tube, measured directly, increases with $\cos(\theta)$. From the individual values, the deformations of the tube can be quantified by calculating R. The dashed line in Figure 5D corresponds to $R = 0.50 \pm 0.02$ indicating a half-cylindrical structure which appears when the tube grows vertically upward, i.e., $\cos(\theta) = 0$ (Fig. 5F). When we tilt the container in the $x-z$ plane (see Fig. 1B), the buoyant forces acting on the membrane distort the originally symmetric structure. If the tilt angle $\theta < 90°$, i.e., $\cos(\theta) > 0$, the tube elongates along

its depth and R becomes greater than 0.5 (Fig. 5E). However, in the opposite scenario, the smaller value of R suggests that the elongation occurs in-diameter (Fig. 5G).

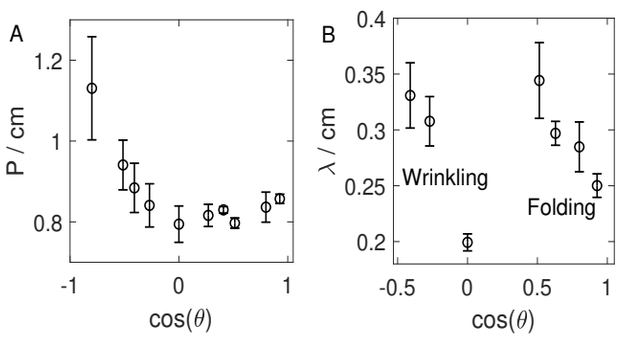

FIG. 6. (A) Perimeter P of the tube and (B) pattern wavelength λ as a function of $\cos(\theta)$ for LMW with $Q = 0.6$ mL min^{-1}.

The volume growth rate calculated from Eqn. (1) is close to the experimentally set injection rate $Q = 0.6$ mL min^{-1} (see Figure S2 in SI), which indicates no liquid transfer across the chitosan membranes. Since the evolving tubes resemble half of elliptical tubes, we can characterize them with their perimeters as

$$P \approx \frac{\pi}{2}\left(3(r+h) - \sqrt{(3r+h)(r+3h)}\right), \qquad (6)$$

using Ramanujan's formula for approximating the circumference of a half ellipse with $r = d/2$ corresponding to the major and h to the minor axis or *vice versa*. Figure 6A displays that the increase in $\cos(\theta)$ below 0 causes the sharp decrease in perimeter, but above zero, no significant variation occurs. The characteristic wavelength of folds and wrinkles, as shown in Fig. 6B, decreases monotonically with $\cos(\theta)$. The angle of these deformations transverse to the tube growth increases with v_ℓ. The deformation path becomes longer as the perimeter increases. The linear growth rate decreases for the wrinkling patterns, but the perimeter increases introducing an opposite influence. The decrease in the wavelength of the wrinkles with $\cos(\theta)$ expresses that the perimeter has a major contribution compared to v_ℓ. Folding patterns, however, deform from both edges simultaneously, and the monotonic decrease in their wavelength is accompanied by decreasing the linear growth velocity.

IV. CONCLUSIONS

Sol-gel transition yields single and multiple chitosan tubules when they are grown horizontally on the bottom of a container. Depending on the injection rate of the CS sol, spontaneous symmetry breaking creates various types of surface instabilities. The linear growth velocity is found to be independent of the flow rates and results in no significant change in the characteristic wavelength of folding patterns. In the case of inclined orientation, increasing the container angle transforms the folding patterns into wrinkles and finally to a tube with smooth outer surface. Close to the vertical orientation, i.e., near 90° tilt angle, and above 90° the linear growth velocity follows a linear scaling as a function of the axial buoyant force and it also plays a significant role in controlling the pattern wavelength. In short, the self-organization of chitosan tube with radial to transverse distortion, is achieved by varying the orientation only. Our present work adds a simple method to the preparation tools of adaptive soft materials and is useful in understanding surface deformations of thin membranes at an interface between two fluids due to physicochemical gradients.

V. SUPPLEMENTARY MATERIAL

See supplementary material for two figures: Figure S1 with comparison of R for various conditions and Figure S2 showing injection rate as a function of the orientation.

VI. ACKNOWLEDGMENT

This work was supported by the National Research, Development and Innovation Office (K138844). Project no. TKP2021-NVA-19 has been implemented with the support provided by the Ministry of Innovation and Technology of Hungary from the National Research, Development and Innovation Fund, financed under the TKP2021-NVA funding scheme.

DATA AVAILABILITY STATEMENT

The data that support the findings of this study are available from the corresponding author upon reasonable request.

[1]Z. L. Wu and J. P. Gong, "Hydrogels with self-assembling ordered structures and their functions," NPG Asia Mater. **3**, 57–64 (2011).
[2]L. M. Barge, S. S. S. Cardoso, J. H. E. Cartwright, G. J. T. Cooper, L. Cronin, A. D. Wit, I. J. Doloboff, B. Escribano, R. E. Goldstein, F. Haudin, D. E. H. Jones, A. L. Mackay, J. Maselko, J. J. Pagano, J. Pantaleone, M. J. Russell, C. I. Sainz-Diaz, O. Steinbock, D. A. Stone, Y. Tanimoto, and N. L. Thomas, "From chemical gardens to chemobrionics," Chem. Rev. **115**, 8652–8703 (2015).
[3]E. Nakouzi and O. Steinbock, "Self-organization in precipitation reactions far from the equilibrium," Sci. Adv. **2**, e1601144 (2016).
[4]S. S. S. Cardoso, J. H. E. Cartwright, J. Cejková, L. Cronin, A. De Wit, S. Giannerini, D. Horváth, A. Rodrigues, M. J. Russel, C. I. Sainz-Díaz, and Á. Tóth, "Chemobrionics: From self-assembled material architectures to the origin of life," Artif. Life **26**, 315–326 (2020).
[5]D. Takács, G. Schuszter, D. Sebők, Á. Kukovecz, D. Horváth, and Á. Tóth, "Magnetic-field-manipulated growth of flow-driven precipitate membrane tubes," Chem. Eur. J. **25**, 14826–14833 (2019).
[6]S. Thouvenel-Romans and O. Steinbock, "Oscillatory growth of silica tubes in chemical gardens," J. Am. Chem. Soc. **125**, 4338–4341 (2003).
[7]V. Kaminker, J. Maselko, and J. Pantaleone, "The dynamics of open precipitation tubes," J. Chem. Phys. **140**, 244901 (2014).
[8]B. C. Batista and O. Steinbock, "Chemical gardens without silica: The formation of pure metal hydroxide tubes," Chem. Commun. **51**, 12962–12965 (2015).

[9]E. Rauscher, G. Schuszter, B. Bohner, A. Tóth, and D. Horváth, "Osmotic contribution to the flow-driven tube formation of copper–phosphate and copper–silicate chemical gardens," Phys. Chem. Chem. Phys. **20**, 5766–5770 (2018).
[10]F. Haudin, J. H. Cartwright, F. Brau, and A. De Wit, "Spiral precipitation patterns in confined chemical gardens," Proc. Natl. Acad. Sci. USA **111**, 17363–17367 (2014).
[11]F. Brau, F. Haudin, S. Thouvenel-Romans, A. De Wit, O. Steinbock, S. S. Cardoso, and J. H. Cartwright, "Filament dynamics in confined chemical gardens and in filiform corrosion," Phys. Chem. Chem. Phys. **20**, 784–793 (2018).
[12]G. Pampalakis, "The generation of an organic inverted chemical garden," Chem. Eur. J **22**, 6779–6782 (2016).
[13]P. Kumar, D. Horváth, and Á. Tóth, "Bio-inspired flow-driven chitosan chemical gardens," Soft Matter **16**, 8325–8329 (2020).
[14]A. Fogde, S. Qudsia, T.-A. Le, T. Sandberg, and T.-P. Huynh, "(calcium-phosphate)/carrageenan gardens grown from the gel/liquid interface," ChemSystemsChem **3**, e2000064 (2021).
[15]E. A. B. Hughes, T. E. Robinson, R. J. A. Moakes, M. Chipara, and L. M. Grover, "Controlled self-assembly of chemical gardens enables fabrication of heterogeneous chemobrionic materials," Commun. Chem. **4**, 145 (2021).
[16]P. Kumar, D. Sebők, A. Kukovecz, D. Horváth, and Á. Tóth, "Hierarchical self-assembly of metal-ion-modulated chitosan tubules," Langmuir **37**, 12690–12696 (2021).
[17]M. Guvendiren, S. Yang, and J. A. Burdick, "Swelling-induced surface patterns in hydrogels with gradient crosslinking density," Adv. Funct. Mater. **19**, 3038–3045 (2009).
[18]T. Tanaka, S.-T. Sun, Y. Hirokawa, S. Katayama, J. Kucera, Y. Hirose, and T. Amiya, "Mechanical instability of gels at the phase transition," Nature **325**, 796–798 (1987).
[19]Y. Tokudome, H. Kuniwaki, K. Suzuki, D. Carboni, G. Poologasundarampillai, and M. Takahashi, "Thermoresponsive wrinkles on hydrogels for soft actuators," Adv. Mater. Interf. **3**, 1500802 (2016).
[20]J. Kim, J. Yoon, and R. C. Hayward, "Dynamic display of biomolecular patterns through an elastic creasing instability of stimuli-responsive hydrogels," Nat. Mater. **9**, 159–164 (2010).
[21]W. Toh, Z. Ding, T. Y. Ng, and Z. Liu, "Light intensity controlled wrinkling patterns in photo-thermal sensitive hydrogels," Coupled Syst. Mech **5**, 315–327 (2016).
[22]D. Chandra and A. J. Crosby, "Self-wrinkling of uv-cured polymer films," Adv. Mater. **23**, 3441–3445 (2011).
[23]X. Cheng and Y. Zhang, "Micro/nanoscale 3d assembly by rolling, folding, curving, and buckling approaches," Adv. Mater. **31**, 1901895 (2019).
[24]E. Kotopoulo, M. Lopez-Haro, J. J. C. Gamez, and J. M. García-Ruiz, "Nanoscale anatomy of iron-silica self-organized membranes: Implications for prebiotic chemistry," Angew. Chem. Int. Ed. **60**, 1396–1402 (2021).
[25]R. Huang and S. H. Im, "Dynamics of wrinkle growth and coarsening in stressed thin films," Phys. Rev. E **74**, 026214 (2006).
[26]E. Cerda and L. Mahadevan, "Geometry and physics of wrinkling," Phys. Rev. Lett. **90**, 074302 (2003).
[27]L. Pocivavsek, R. Dellsy, A. Kern, S. Johnson, B. Lin, K. Y. C. Lee, and E. Cerda, "Stress and fold localization in thin elastic membranes," Science **320**, 912–916 (2008).
[28]F. Brau, P. Damman, H. Diamant, and T. A. Witten, "Wrinkle to fold transition: influence of the substrate response," Soft Matter **9**, 8177–8186 (2013).
[29]D. P. Holmes and A. J. Crosby, "Draping films: A wrinkle to fold transition," Phys. Rev. Lett. **105**, 038303 (2010).
[30]P. Ciarletta, "Wrinkle-to-fold transition in soft layers under equi-biaxial strain: A weakly nonlinear analysis," J. Mech. Phys. Solids **73**, 118–133 (2014).
[31]Y. Ebata, A. B. Croll, and A. J. Crosby, "Wrinkling and strain localizations in polymer thin films," Soft Matter **8**, 9086–9091 (2012).
[32]J. Yin, Z. Cao, C. Li, I. Sheinman, and X. Chen, "Stress-driven buckling patterns in spheroidal core/shell structures," Proc. Natl. Acad. Sci. USA **105**, 19132–19135 (2008).
[33]K. Efimenko, M. Rackaitis, E. Manias, A. Vaziri, L. Mahadevan, and J. Genzer, "Nested self-similar wrinkling patterns in skins," Nat. Mater. **4**, 293–297 (2005).
[34]V. Fernández, C. Llinares-Benadero, and V. Borrell, "Cerebral cortex expansion and folding: what have we learned?" EMBO J. **35**, 1021–1044 (2016).
[35]K. D. Walton, Å. Kolterud, M. J. Czerwinski, M. J. Bell, A. Prakash, J. Kushwaha, A. S. Grosse, S. Schnell, and D. L. Gumucio, "Hedgehog-responsive mesenchymal clusters direct patterning and emergence of intestinal villi," Proc. Natl. Acad. Sci. USA **109**, 15817–15822 (2012).
[36]Y. Tan, B. Hu, J. Song, Z. Chu, and W. Wu, "Bioinspired multiscale wrinkling patterns on curved substrates: An overview," Nanomicro Lett. **12**, 1–42 (2020).
[37]P. Ciarletta, V. Balbi, and E. Kuhl, "Pattern selection in growing tubular tissues," Phys. Rev. Lett..
[38]P. Kumar, C. Hajdu, Á. Tóth, and D. Horváth, "Flow-driven surface instabilities of tubular chitosan hydrogel," ChemPhysChem **22**, 488 (2021).

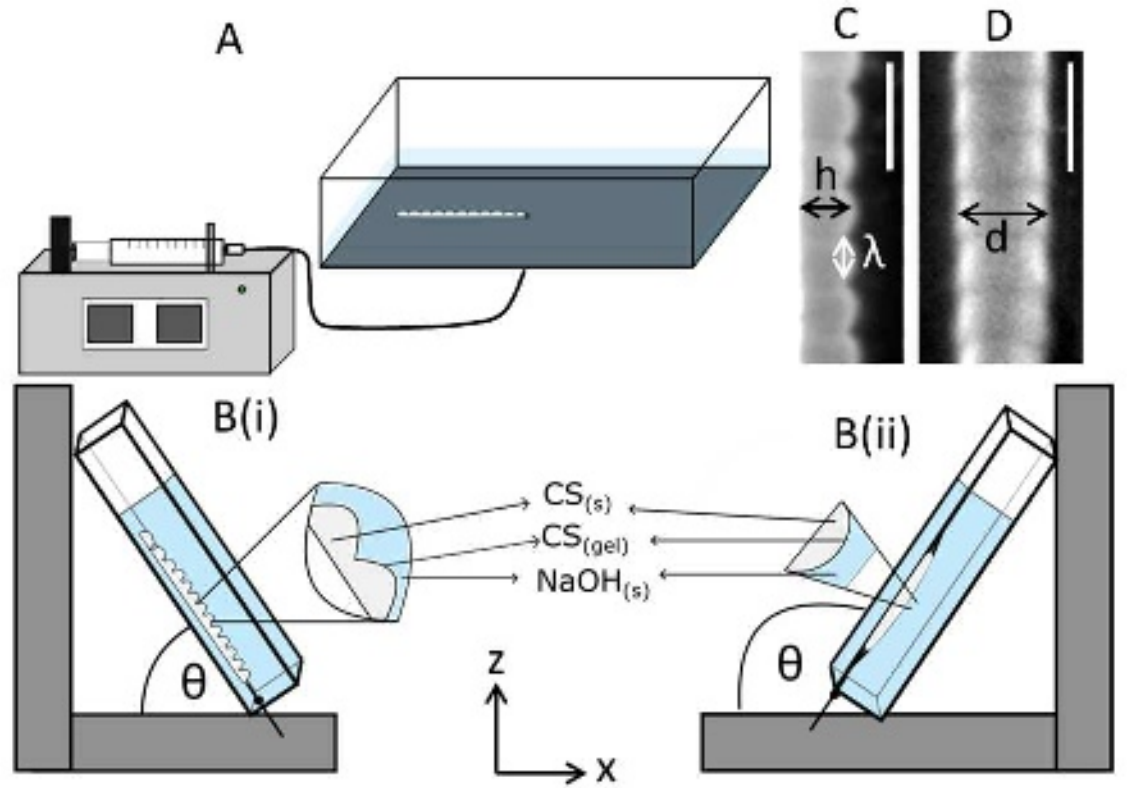
A
C
D
h
λ
d
B(i)
B(ii)
CS(s)
CS(gel)
NaOH(s)
θ
θ
z
x

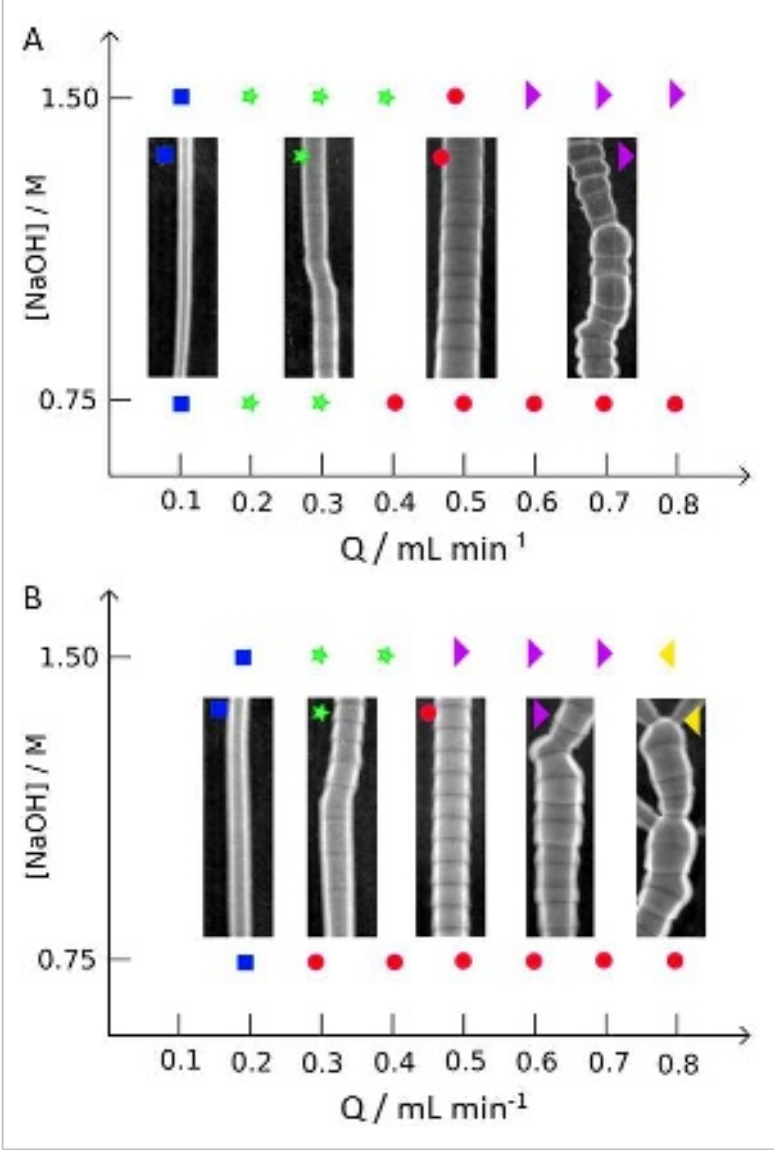
A
1.50
[NaOH] / M
0.75
0.1 0.2 0.3 0.4 0.5 0.6 0.7 0.8
Q / mL min 1
B
1.50
[NaOH] / M
0.75
0.1 0.2 0.3 0.4 0.5 0.6 0.7 0.8
Q / mL min-1

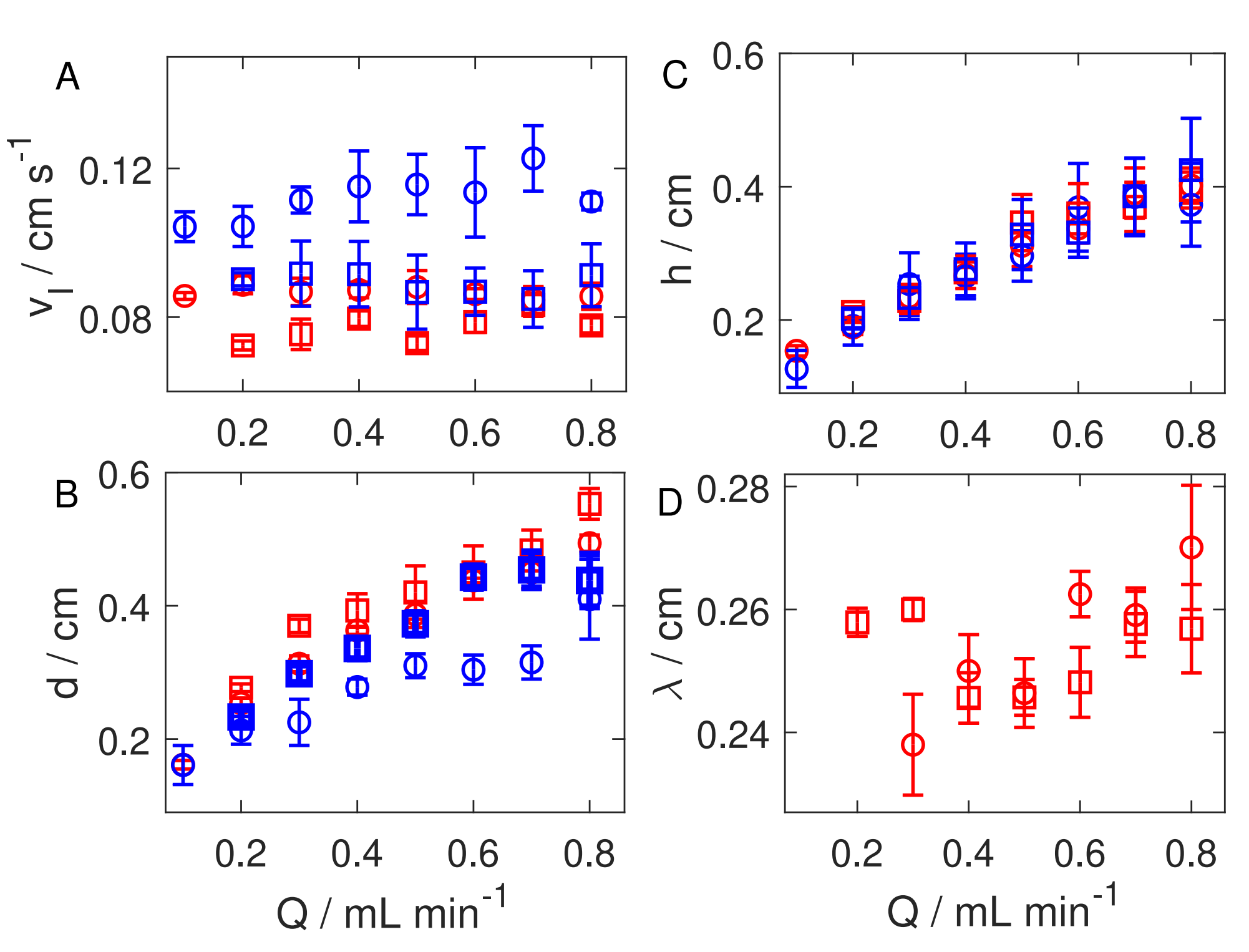
A
B
C
D
v_l / cm s^{-1}
d / cm
h / cm
λ / cm
Q / mL min^{-1}
Q / mL min^{-1}
0.08
0.12
0.2
0.4
0.6
0.24
0.26
0.28
0.2
0.4
0.6
0.8

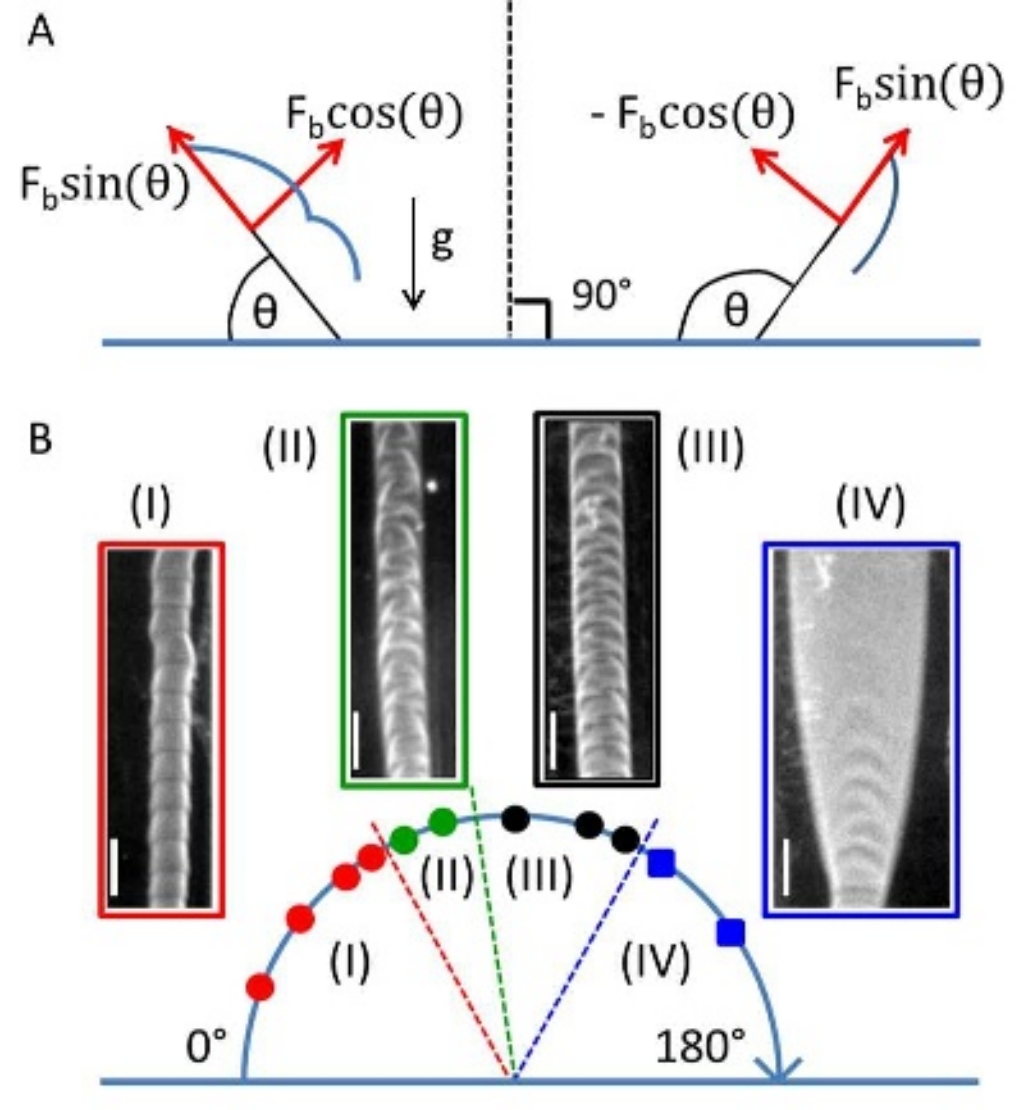
A
$F_b\cos(\theta)$
$F_b\sin(\theta)$
g
θ
90°
$-F_b\cos(\theta)$
$F_b\sin(\theta)$
θ
B
(I)
(II)
(III)
(IV)
(I)
(II)
(III)
(IV)
0°
180°

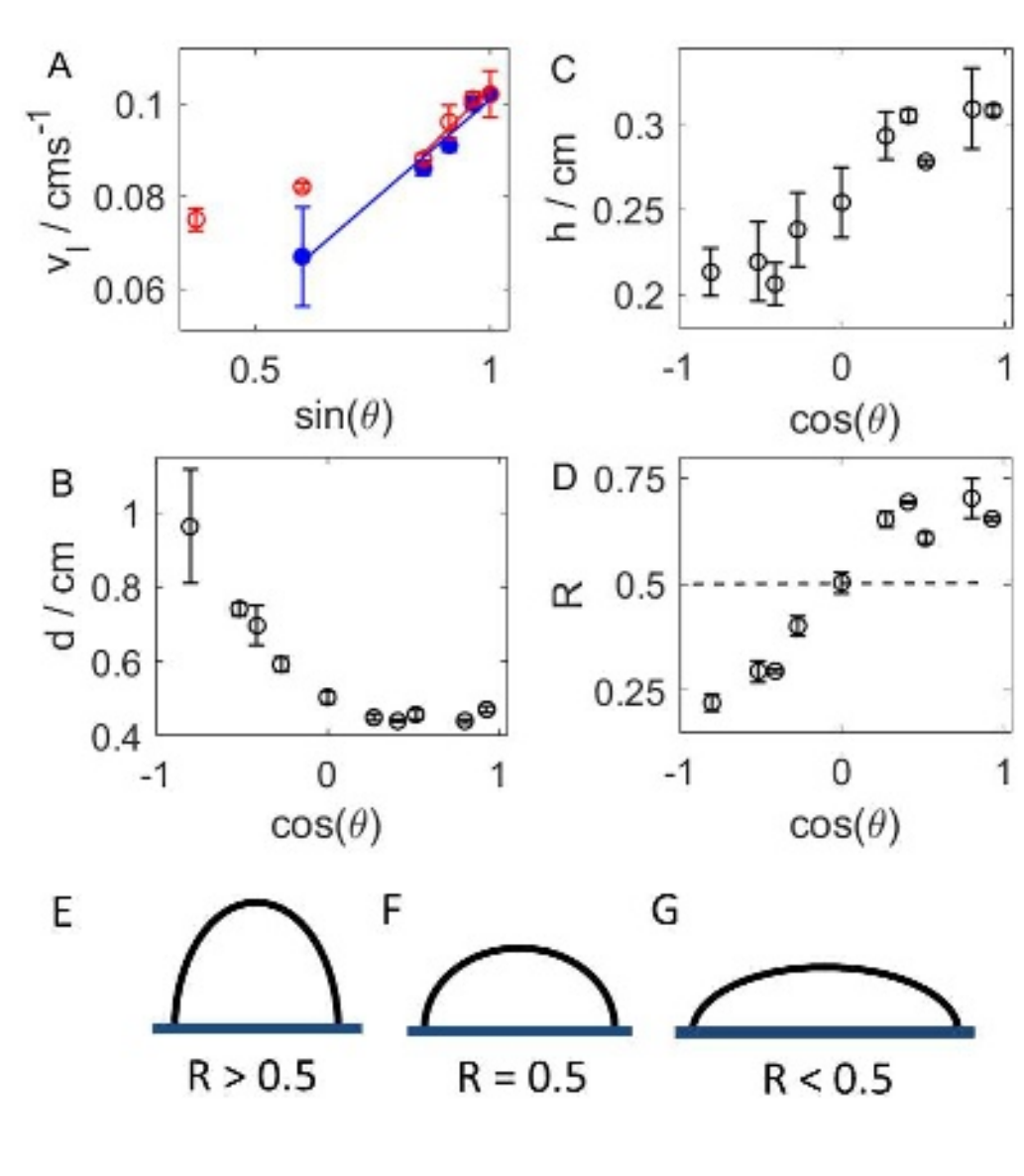
A
v_l / cms^{-1}
0.1
0.08
0.06
0.5
1
sin(θ)
C
h / cm
0.3
0.25
0.2
-1
0
1
cos(θ)
B
d / cm
1
0.8
0.6
0.4
-1
0
1
cos(θ)
D
R
0.75
0.5
0.25
-1
0
1
cos(θ)
E
R > 0.5
F
R = 0.5
G
R < 0.5

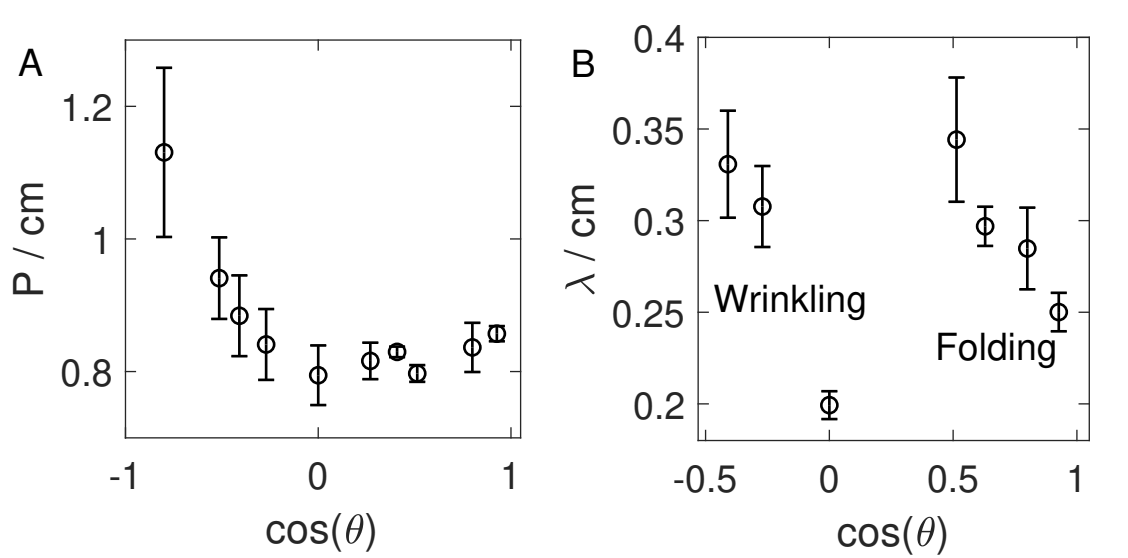
A
P / cm
1.2
1
0.8
-1
0
1
cos(θ)
B
λ / cm
0.4
0.35
0.3
0.25
0.2
Wrinkling
Folding
-0.5
0
0.5
1
cos(θ)